

Breakdown of the Linear Physical Behavior in a Solid Solution of a Halometallate Molten Salt, (dimim)[Fe(Cl_{1-x}Br_x)₄] $0 \leq x \leq 1$.

Palmerina González-Izquierdo,^{*1,2} Oscar Fabelo,^{*1}, Israel Cano,³ Oriol Vallcorba,⁴ Jesús Rodríguez Fernández,¹ María Teresa Fernández-Díaz² and Imanol de Pedro^{*1}

¹ CITIMAC, Facultad de Ciencias, Universidad de Cantabria, 39005 Santander.

² Institut Laue-Langevin, BP 156X, F-38042 Grenoble Cedex, France.

³ School of Chemistry, University of Nottingham, NG7 2RD, Nottingham, UK.

⁴ ALBA Synchrotron Light Source, Cerdanyola del Vallés, Barcelona, Spain.

Corresponding Authors: e-mails: depedrovm@unican.es; fabelo@ill.fr; gonzalez-izquierdo@ill.fr

Abstract:

Sixteen samples of the (dimim)[Fe(Cl_{1-x}Br_x)₄] $0 \leq x \leq 1$ solid solution were prepared in a one-pot synthesis. Single crystal and synchrotron X-ray powder diffraction studies show that all compounds are isomorphous with an orthorhombic structure (*Ama2* space group) at room temperature. The crystal structure of these imidazolium molten salts can be described as layers of (dimim)⁺ cations (dimim=1,3-dimethyl-imidazolium) extended in the *bc*-plane with an antiparallel stacking along the *a*-axis forming a herring-bond motive. The (FeX₄)⁻ (X = Cl and Br) anions form layers extended on the *bc*-plane that are intercalated between the organic layers and inverted with respect to the adjacent layer along the *a* direction. The evolution of the cell volume at this temperature follows the Vegard's law in the whole range of substitution with $\Delta V \approx 115 \text{ \AA}^3$ between non-substituted phases, showing a non-linear axial expansion in the *b* and *c* directions. In addition, the melting point of the solid solution does not follow the expected linear physical behavior. Finally, the magnetic study indicates the existence of overall antiferromagnetic interactions as predominant, which are stronger with the increase in the (FeBr₄)⁻ ion substitution. However, it was found that the 3D magnetic ordering of the non-substituted phases vanishes or it is below the minimum temperature reachable by the magnetometer devices (1.8 K) for the 25-50% bromide substitutions. This is connected with the appearance of different crystal phases as function of bromide composition at low temperature.

Keywords: imidazolium molten salts; halometallate solid solution; structure elucidation, thermophysical and magnetic properties.

Contents

1. Introduction
 2. Experimental section
 3. Synthesis and chemical analysis
 4. Structural and thermal characterization
 5. Magnetic studies
 6. Conclusion
- Associated Content
Acknowledgment
References

1. Introduction

Halometallate compounds, synthesized by the reaction of a metal halide with an organic salt, display very interesting features that depend on the different ionic building blocks, such as strong Lewis acidity,[1,2] paramagnetism,[3,4] thermo/photo-chromism,[5] high thermal stability and wide electrochemical window.[6] This range of properties offers numerous and promising technological applications like energy storage,[7,8] transport and separation of metals and materials,[9,10] separation of greenhouse gases,[11,12] magnetic surfactants,[13] extraction of DNA,[14] production of biodiesel by esterification of acid oleic,[15] catalysis,[16-18] semiconductor nanocrystals[19] or hydrocarbon processes using halometallate ionic liquid micro-emulsions.[20]

In these materials, the most usual way to tune physical features such as thermal, optical and magnetic properties, Lewis acidity or ionic conductivity is to change the alkyl chain (R) length in the organic cation and/or the total substitution of the halides (X) in the metal complex anion.[21] A recent new strategy is to synthesize double halometallate salts,[22] that include at least one organic cation and two metal halide anions, which also allows fine-tuning these properties depending on their anionic speciation and ratio. The synthesis process is based on the addition of a given amount of a metal halide, MX_n , to a halide-based ionic liquid, $[cat]X$, resulting in a mixture which may contain a halide and one or more halometallate anions in a dynamic equilibrium with the cation. This equilibrium constitutes a fundamental characteristic of the double halometallate salt, where the anionic speciation can be complex and exhibit interesting technological applications.[23] Thus, as it was commented in two recent interesting reviews,[24,25] each double halometallate salt is a unique system that may not follow the expected linear physical behavior of an ideal homogeneous mixture.[26] For instance, double halometallate salts containing 1-butyl-3-methyl-imidazolium (bimim), which is a common cation in several binary mixtures, usually presents very small deviations in the molar volume while large deviations are detected in the viscosity.[27] In contrast, the mixture of two chlorometallate anions based on iron and gadolinium with 1-ethyl-3-methyl-imidazolium (emim) follows an ideal behavior in the magnetic and conductivity properties.[28]. Therefore, physical and chemical properties that are dependent on the chemical associations between the ions, or altering the ionic ratios in the double halometallate salts can induce different chemical interactions leading to new properties or a non-ideal behavior.

Interestingly, we have observed that the partial substitution of halide anions in a halometallate molten salt based on imidazolium cation has not yet been investigated in depth. In this context, $(dimim)[FeCl_4]$ and $(dimim)[FeBr_4]$ are isomorphous at room temperature (RT), [29, 30] and thus a solid solution of both compounds could be generated. Consequently, we have prepared a solid-solution of sixteen samples of $(dimim)[Fe(Cl_{1-x}Br_x)_4]$ ($dimim=1,3$ -dimethylimidazolium), x ranging from 0 to 1 by a straightforward one-pot synthesis. In this line, the crystal structures of

(dimim)[FeX₄] (X = Cl and Br) were previously determined by synchrotron X-ray powder diffraction (SR-XRPD) at RT, as monoclinic systems (*P*2₁ symmetry). However, as it will be discussed hereafter, after the single crystal diffraction analysis of (dimim)[Fe(Cl_{0.5}Br_{0.5})₄] and re-examination of the SR-XRPD data for the non-substituted compounds and the new 16 samples of the solid solution, it was demonstrated that all compounds are isomorphous and crystallize in an orthorhombic structure (*Ama*2 symmetry). Therefore, we decided to study in detail the variation of some physical properties of the solid solution with the halide substitution degree. Remarkably, the melting point and the magnetic properties do not follow the expected linear physical behavior; i.e. the 3D magnetic ordering of (dimim)[FeX₄] (X = Cl and Br) vanishes or it is below 1.8 K for 25-50% of bromide substitution. This behavior is totally different from that observed in the dilution of (emim)[FeCl₄] with an equimolar amount of a non-magnetic ionic liquid, (emim)[GaCl₄].[28] Indeed, this solid solution of a halometallate molten salt acts as a unique system that does not follow the expected physical performance.

2. Experimental section

2.1. General procedures

Solvents were purchased from Sigma-Aldrich as HPLC grade and dried by means of an Inert Puresolv MD purification system. All reagents were purchased from commercial suppliers (Sigma Aldrich and Acros). The ion exchange resin Amberlite IRA-402(OH) was supplied by Alfa Aesar.

2.2. Elemental analysis (EA)

Elemental analyses were performed by the elemental analysis service of the University of Nottingham.

2.3. Thermal analysis

A Setaram calorimeter (DSC131) was used for the thermal analyses from RT to 393 K under nitrogen atmosphere at a heating rate of 10 K/min. For this experiment, *ca.* 5 mg of sample were used, and blank runs were performed.

2.4. X-ray powder diffraction data collection

The purity of the samples was evaluated by X-ray powder diffraction (XRPD) under air atmosphere on a Bruker D8 Advance diffractometer, using Cu K α radiation ($\lambda = 1.54178 \text{ \AA}$) and a LynxEye detector. Diffraction patterns were collected with an angular 2θ range between 10 and 50° with a 0.02° step size, measurement time of 3 s per step and a graphite monochromator. The instrumental resolution function (IRF) of the diffractometer was obtained from the LaB₆ standard.

2.5 Single crystal X-ray diffraction

A dark red plate-like specimen of (dimim)[FeCl_{0.5}Br_{0.5}]₄ (Cl/Br 50%) with approximate dimensions 0.07 mm x 0.07 mm x 0.05 mm was used for the X-ray crystallographic analysis on the dual-source D8 Venture equipped with a Photon III detector operated at 296.0(2) K. The Copper μ -source was used providing X-rays with a wavelength of $\lambda = 1.54178 \text{ \AA}$. The data reduction was performed with the Bruker SAINT software package [31] using a narrow-frame algorithm. The data integration using an orthorhombic unit cell, $a = 14.1882(11) \text{ \AA}$, $b = 9.4425(10) \text{ \AA}$, $c = 9.3989(12) \text{ \AA}$, with a volume of $1259.2(2) \text{ \AA}^3$, yielded a total of 7096 reflections to a maximum θ angle of 79.824° . Data were

corrected for absorption effects using the Multi-Scan method (SADABS).[32] All the structures were solved and refined with the Bruker SHELXTL Software Package,[33] using the space group *Ama2*, with $Z = 4$ for the formula unit, $(\text{dimim})[\text{FeCl}_2\text{Br}_2]$. The final full-matrix least-squares refinement on F^2 with 64 variables converged at $R_1 = 9.85\%$, $wR_2 = 25.53\%$ for $2\sigma(F^2)$ data. The goodness-of-fit was 1.631. All non-hydrogen atoms were refined anisotropically. However, it is worth noting that large anisotropic displacement parameters in both cationic and anionic units have been observed due to the weak-bonding nature of the compound.

2.6. Synchrotron X-ray powder data collection and structure refinement:

Synchrotron X-ray powder diffraction (SR-XRPD) measurements at 300, 100 and 80 K were performed at the high resolution station of the MSPD beamline (BL04) at ALBA synchrotron.[34] The sample was introduced into a 0.7 mm glass capillary and measured in transmission at an energy of 20 keV (0.61970(3) Å wavelength determined from a Si NIST-640d reference) using the microstrip Mythen-II detector (six modules, 1280 channels/module, 50 μm/channel, sample-to-detector distance 550 mm). Initially, the temperature was controlled using an Oxford Cryostream Series 700 and the sample were cooled down to below 110 K via thermal quenching (at 5 K/min). The crystal structures of 15 selected samples of the solid solution at R.T. were refined using the Rietveld method with the FullProf suite program,[35] starting from the single-crystal structure model of $(\text{dimim})[\text{FeCl}_{0.5}\text{Br}_{0.5}]_4$ and from those models previously reported for the parent phases at low temperature. All the refinements were performed using the rigid body formalism, by fixing the structure of the organic cation and the inorganic anion and allowing them to move and rotate within the cell without modifying their internal distances. Two tetrahedra of FeCl_4 and FeBr_4 were included with the same coordinates sharing the occupation of each atom. The Debye Waller factors were refined isotropically by groups of atoms, i.e. C and N atoms were assigned the same factor, as well as all the Cl/Br atoms. The occupation of the Cl and Br atoms were refined together with the sum of both components restricted to have the occupancy of the Wyckoff site.

2.7 Magnetization measurements

DC magnetic susceptibility measurements were performed using a Quantum Design QPMS magnetometer between 2 and 300 K under an applied magnetic field of strength 1 kOe. Magnetization as a function of field (H) was measured using the same magnetometer in the $-50 \leq H/\text{kOe} \leq 50$ range at 2 K after cooling the sample in zero field. In a previous work it was observed that $(\text{dimim})[\text{FeCl}_4]$ shows two interesting phase transitions depending on the cooling process [36]; via thermal quenching or via slow cooling with $T < 2\text{K}/\text{min}$ [named in this work as phase **I-a**: space group $P2_12_12_1$ with $a = 9.1242(1)$, $b = 13.8132(2)$, $c = 9.0359(1)$ Å and phase **I-b**: space group $P2_1/c$ with $a = 14.1391(3)$, $b = 13.7039(3)$, $c = 13.2935(3)$ Å, $\beta = 115.539(2)^\circ$] (Figure S1). All structures exhibit a long-range antiferromagnetic ordering at low temperatures, determined by high- and low-resolution neutron diffraction experiments, with Neel temperatures of 3.1 K (**I-a**) and 5.4 K (**I-b**). Therefore, to compare the magnetic results with those of the parent phases, the samples of the solid solution were quenched from RT to 100 K using the SQUID cryostat in order to obtain the “quenched” phase. Later, the temperature was then cooled down to 2 K in zero field (ZFC) mode and the magnetization was measured at this temperature. After that, ZFC-FC magnetic susceptibility measurements were performed from 2 to 20 K under 1 kOe following of ZFC magnetic susceptibility measurements at 1 kOe from 2 to 220 K. Later, the sample was kept constant at this temperature for 1 h without applying any magnetic field to induce the transformation of the quenched phase into the “relaxed” phase. After this protocol the temperature was then cooled down to 2 K, and the same magnetic measurements as for the quenched phase were carried out. On the other hand, heat capacity measurements were performed through a relaxation method using a

Quantum Design PPMS system. The sample consists of a plate of 0.3 mm thickness and *ca.* 5 mg weight obtained by compressing the original polycrystalline powder. In order to ensure good thermal contact, the sample was glued to the sample holder using Apiezon-N grease. Data were collected with zero field and under an applied field of 80 kOe from 2 to 300 K.

3. Synthesis and chemical analysis

The synthesis of 1,3-dimethylimidazolium chloride, (dimim)[Cl] was realized following a previously used method for (dimim)[FeCl₄].[30] 1,3-dimethylimidazolium bromide was prepared in the same way, except for the use of hydrobromic acid (47%, Vetec) in place HCl. For (dimim)[FeCl_{1-x}Br_x]₄ 0.025 ≤ *x* ≤ 0.95, (dimim)[Cl] was mixed with a mixture of stoichiometric amounts of anhydrous FeX₃ (X = Cl and Br) in a 8 mL vial inside the glove-box, (see Table S1). For lower percentages (0.20 ≥ *x* ≥ 0.05), (dimim)[Br] was used. The resulting mixture was heated up to 393 K and the desired product was obtained as a brown-reddish solid, 3 g (100% yield). The microanalytical data (C, H and N, Fe, Br and Cl) were in good agreement with the expected one (Table S2).

4. Structural and thermal characterization

XRPD and SR-XRPD measurements at RT were performed to study the purity of the samples and to obtain the cell parameters of the solid solution (Figure S2). The crystal structure of 15 selected samples of the solid solution was refined from SR-XRPD (Figure S3). We have not SR-XRPD crystallographic data of (dimim)[FeCl_{1-x}Br_x]₄ (0.25, 0.85 and 0.95) samples due to the lack of time in the high resolution station of the MSPD beamline (BL04) at ALBA synchrotron (proposal nr. 20170923666). The final structural parameters and figures of merit of the last Rietveld refinements are summarized in Table S3. The positional parameters are given in the corresponding CIF files. The cell parameters of the remaining samples were obtained by performing a pattern matching to the XRPD data.

All compounds of the solid solution are isomorphous, crystallizing in the orthorhombic *Ama2* space group. The asymmetric unit (Figure 1) consists of one half of the organic molecule, while the other half is generated by a two-fold rotation axis passing by the C2 atom. The anionic counterpart consists of one Fe and three Cl/Br atoms. The third halogen atom is generated by a mirror plane in which the Fe1, X2 and X3 atoms are located (X can be any Cl/Br ratio).

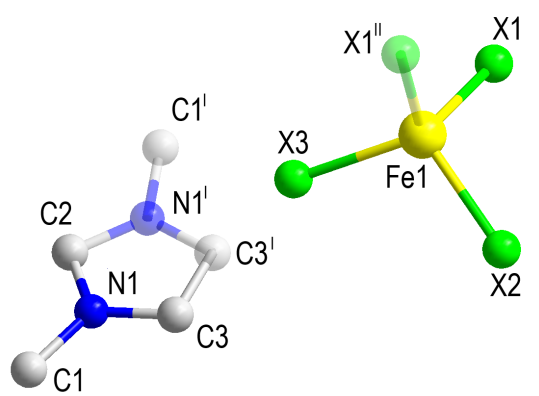


Figure 1: Asymmetric unit of the solid solution samples at RT, where X can be any Cl/Br ratio. Symmetry operations: I: $-x, -y, z$; II: $3/2-x, y, z$.

The volume of the unit cell in the orthorhombic space group (*Ama2*) is approximately two times the volume of the previously described monoclinic unit cell (*P2₁*) for the non-substituted phases.[29,30] The transformation between cells follows the next equation: $a'=-b-c$, $b'=a$, $c'=b-c$ plus a global offset which corresponds to a rotation of 45 deg. with respect to the long axis (see detail in Figure 2). Structurally, the difference between the orthorhombic structure and that previously described in the *P2₁* space group is the suppression of the antiparallel orientation of the organic molecules along the *b*-direction (*a*-direction in the *Ama2* space group), due to the occurrence of a 2₁ screw axis along the *b*-axis in the monoclinic space group. An overlapping of both structures is shown in Figure 2.

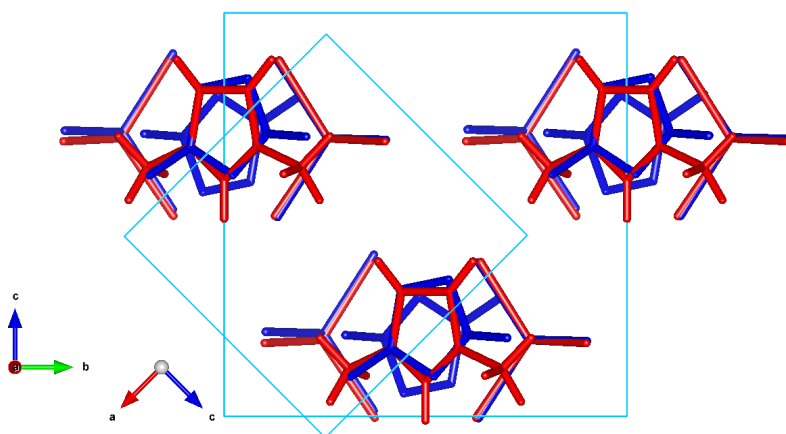


Figure 2: overlapping of the *P2₁* (blue) and *Ama2* (red) structures of the sample with $x=0.5$ bromide content.

The orthorhombic crystal structure, which is present in all the compounds of the solid solution, can be described as layers of $(\text{dimim})^+$ cations and $(\text{FeBr}_4)^-$ anions extended in the *bc*-plane and stacked along the *a*-axis. The organic layers are related by a mirror plane, which is placed between two adjacent layers, giving rise to a herring-bond motive. The $[\text{Fe}(\text{Cl}/\text{Br})_4]^-$ units are located between two adjacent organic layers. A continuous shift in both the cationic and anionic units is observed, which is mainly as a consequence of the variations in the cell parameters produced by the different average ionic radii between the Cl/Br mixtures. This shift can be seen in Figure 3, which displays a comparison between the cells of non-substituted phases.

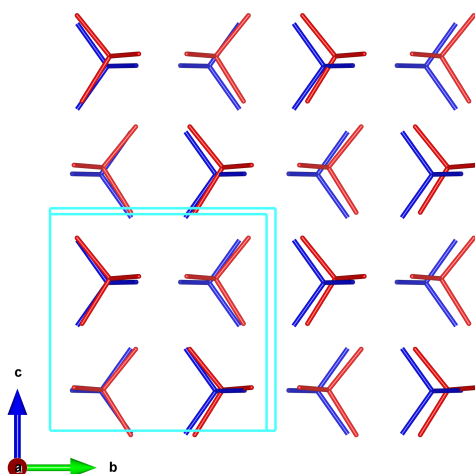


Figure 3: Crystal packing in the *ab*-plane for $(\text{dimim})[\text{FeCl}_4]$ (blue) and $(\text{dimim})[\text{FeBr}_4]$ (red) crystal structures at 300 K. The organic cations have been omitted for the sake of clarity.

The evolution of the crystal parameters as function of halide substitution degree at RT is shown in Figure 4 (left). The cell volume follows the Vegard's law [37] in the entire composition range ($\Delta V \approx 115 \text{ \AA}^3$ between non-substituted phases). While the *a*-axis follows an almost linear tendency, a change in the slope for the *c*-axis is observed, which it is less pronounced along the *b*-axis for values above 40% of bromide substitution. This variation in the slope is also detected in the direction where the Fe···Fe interactions are the shortest, within the *bc*-plane (see Figure 4 right). Therefore, this weak structural anisotropy can be associated to the chemical stress produced by the large bromide ionic radius in comparison with that of chloride. Moreover, the evolution of the shortest halide···halide and Fe···centroid distances (Table S4), considering this distance as an average distance for all possible anion- π interactions in the system, exhibit a linear behaviour (see Figure 4 right).

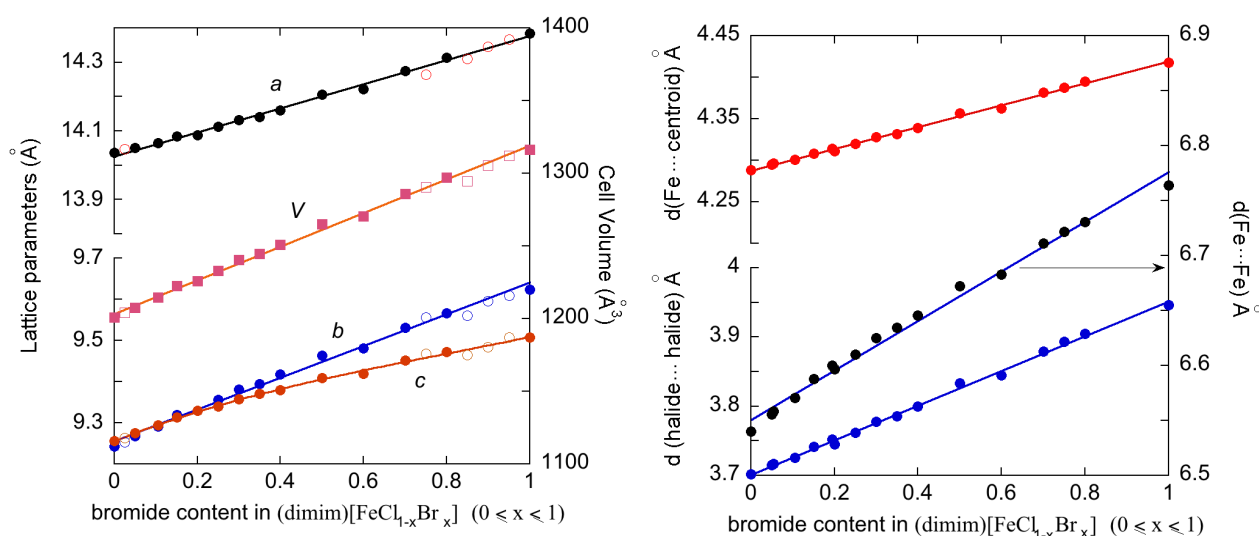


Figure 4: Evolution of the cell parameters (left), volume cell, shortest Fe···Fe, halide···halide and Fe···centroid distances (right) at 300 K. The filled and empty data points correspond to the Rietveld refinement to the SR-XRPD and the pattern matching to the XRPD data, respectively.

SR-XRPD measurements of the solid solution collected below 110 K via thermal quenching (at 5 K/min), suggest the occurrence of different crystal structures as function of bromide composition. A possible explanation of this issue is the occurrence of different relaxation process during the cooling process or to the breaking of cooperativity of the $[\text{Fe}(\text{Cl}/\text{Br})_4]^-$ units (chemical pressure). At low bromide content, 5-25%, the patterns can be successfully refined using the **I-a** crystal structure of pure chloride compound, described on the $P2_12_12_1$ space group (Figure S4). Between 30 and 60% of bromide the best model was refined using the *Ama2* space group (Figure S5). Only a thermal contraction of the R.T. unit cell was included in the refinement, to fit the experimental data properly. Therefore, no-phase transition is observed in this composition range. The phase transition between the two orthorhombic space groups induces a notable modification of the structural parameters. It deserves to be noted that the distances where the Fe···Fe and the Fe···centroid interactions are shorter in the $P2_12_12_1$ than in the *Ama2* space group (see Figure 5). This breaking of symmetry seems to be the origin of the different magnetic behaviour of this series. Above 60% of bromide content, we could not refine the SR-XRPD data using the parent models (phase **I-a** and phase **I-b**). Our best fitting shows the presence of a superstructure which has approximately three times the volume of the previously described orthorhombic unit cell. However, further crystallographic studies are needed to discuss its property. A detailed description of the low temperature magnetic behaviour of all samples of the solid solution will be discussed in the next section.

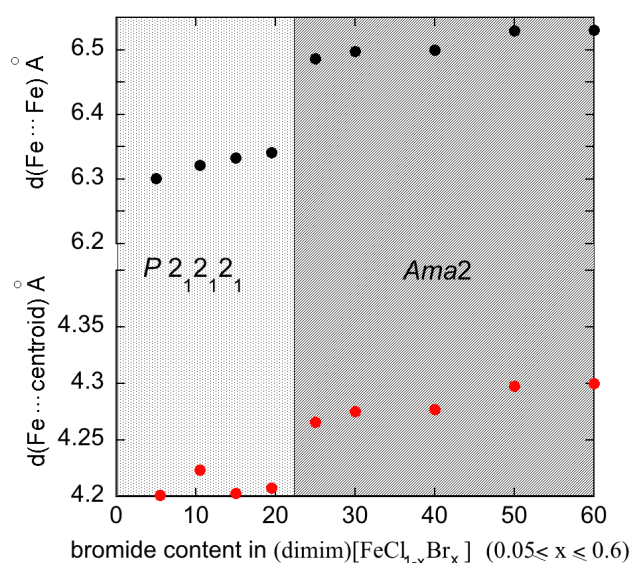


Figure 5: Evolution of the shortest Fe...Fe and Fe...centroid distances at 100 K for (dimim)[Fe(Cl_{1-x}Br_x)₄] 0.05 ≤ x ≤ 0.60.

DSC thermograms from RT to 393 K were acquired to study the evolution of the melting point in (dimim)[Fe(Cl_{1-x}Br_x)₄] (0 ≤ x ≤ 1) (Figure S6). The values of the melting point peak (T_{peak}) and the offset temperature (T_{offset}), defined as the intersection of the tangents of the peak with the extrapolated baseline, are listed in Table S5. All compounds are solid at RT and, except for x = 0.95 and 1 compositions,[29] they do not display solid-solid transitions in this temperature range (inset of Figure S4). T_{offset} is almost constant (between 360 and 365 K) for 0 ≤ x ≤ 0.4 samples. Then, this value increases up to 370.9 K for x = 0.6 composition and subsequently it rises to 376.8 K for x = 0.75. This thermal behavior is consistent with greater interionic interactions in (dimim)[FeBr₄]. However, it suddenly drops down to 365 K for x = 0.8 and rises again up to 369 K for x = 1 (Figure S7). Thus, the melting point of the solid solution does not follow the expected linear physical behavior.

5. Magnetic studies

As commented, the solid phase of (dimim)[FeCl₄], after a thermal quenching, crystallizes in the orthorhombic structure with a three-dimensional antiferromagnetic ordering below 3 K (quenched phase in this manuscript). After a thermal treatment of this phase (see experimental part), a crystal structure transformation to a monoclinic phase takes place, involving a translational and reorientational process of the dimim counterions and [FeCl₄]⁻ anions (relaxed phase) (Figure 1 of Supplementary material).[36] This feature is connected with the modification of the super-exchange pathways, and therefore the magnetic behavior after the solid-to-solid phase transition by thermal effect, which increases the magnetic long-ranged order temperature, T_N from ca. 3 to 5.4 K. In order to follow this interesting dynamical process which could affect to the magnetic properties of the solid solution, magnetometry measurements were performed following the same thermal magnetic study (see experimental part) used for (dimim)[FeCl₄], (Figures S8 and S9). The main magnetic data are shown in Table S6.

In all samples, the linear behavior of χ_m^{-1} at $T > 10$ K can be fitted to a Curie-Weiss law (Figures S8). The effective paramagnetic moment, μ_{eff} , ranges between 5.52 and 6.06 μ_B/Fe ion. These values are in good agreement with the expected one for a Fe^{3+} ion with a magnetic spin $S = 5/2$ (5.92 μ_B) and with those found for other halometallate compounds based on imidazolium and $[\text{FeCl}_4]^-$ and $[\text{FeBr}_4]^-$ ions.[38, 39] The Curie-Weiss temperature, (θ_P), obtained through the fitting, decreases with the $[\text{FeBr}_4]^-$ ions substitution for both phases [from -6.09(1) to -14.29(1) K in the quenched-phase and from -8.5 to -14.09 K in the relaxed-phase], (see Figure S10 left) which denotes stronger antiferromagnetic interactions. Interestingly, at low temperatures the differences between the ZFC curves of both phases decrease with the increase in the ratio of $[\text{FeBr}_4]^-$ ions, and are almost identical for concentrations higher than 25% (Figure 6 left and S8). Likewise, the differences in the field dependence of the magnetization between both phases at 2 K are non-existent (see Figure 6 right and Figure S9). On the other hand, they are anhysteretic which confirm the absence of a ferromagnetic component. The obtained effective moment at 50 kOe decreases from 4.20(1) to 1.18(1) and from 2.91(1) to 1.17(1) μ_B/iron atom for the quenched and relaxed phases, respectively (see Figure S10 right). This feature indicates that, in this solid solution with isotropic exchange interactions [as it is expected for Fe(III)], the small variation in the non-bonding interactions (anion-anion and anion- π interactions) plays an important role in the change of the magnetic behavior of the solid solution with the thermal process.

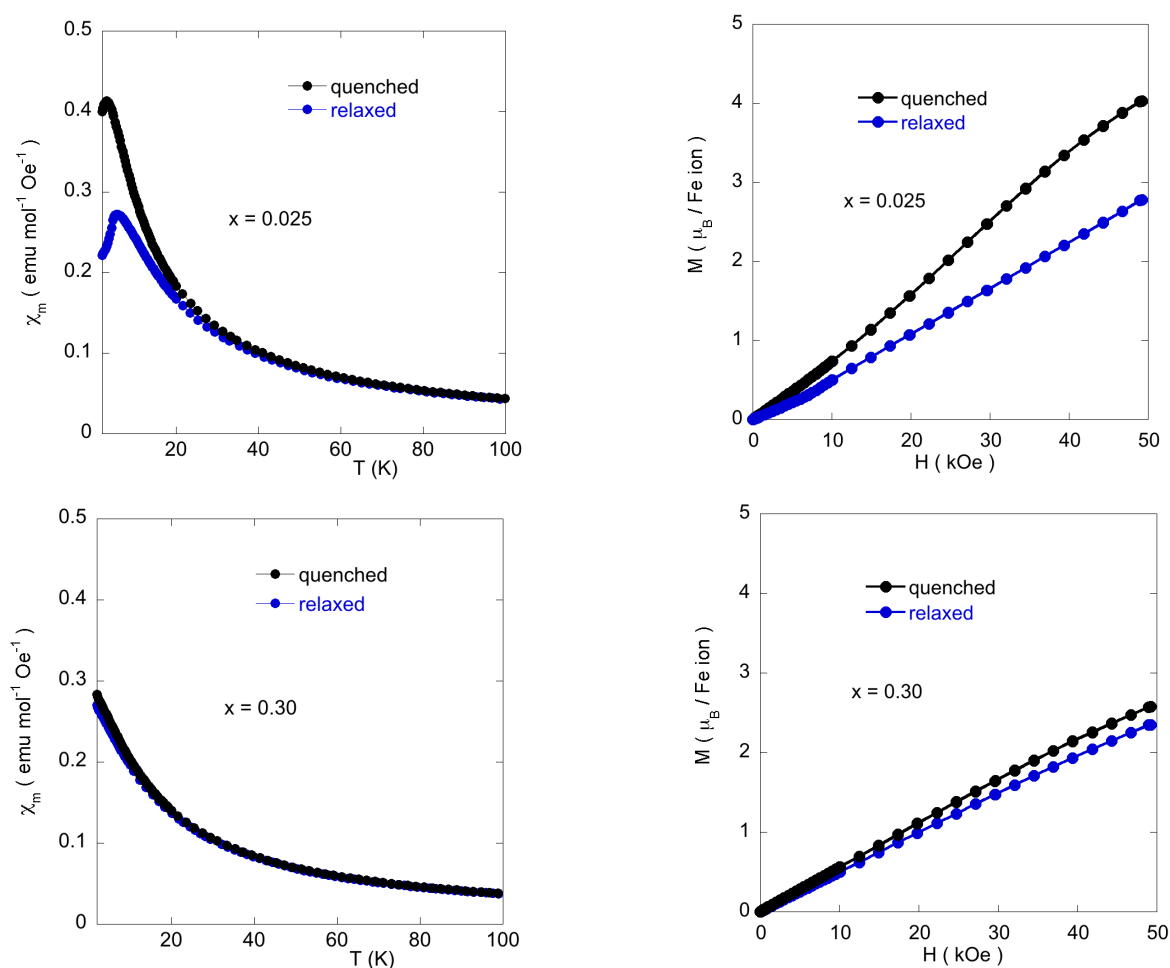


Figure 6. Temperature dependence of χ_m measured under 1 kOe (right) and magnetization at 2K (left) for the quenched (black dots) and relaxed (blue dots) phases of $x = 0.025$ and 0.30 compositions.

As commented, at low temperatures, (dimim)[FeCl₄] displays long-range magnetic ordering at 3.1 and 5.4 K for the quenched and relaxed phases, respectively.[36] Surprisingly, instead of an increase in the Néel temperature (T_N) at higher bromide anion concentrations in the solid solution (up to 7.7 K for $x=1$),[29] we have found that the 3D ordering temperature decreases progressively from 5.5 K until it vanishes or its value is below the minimum temperature reachable by the SQUID device (1.8 K) for $x=0.25$ in both phases (see Figure 7). What is more, the 3D ordering temperature appears again and its value increases for $x > 0.50$. This interesting evolution is plotted in the magnetic phase-diagram shown in Figure 8.

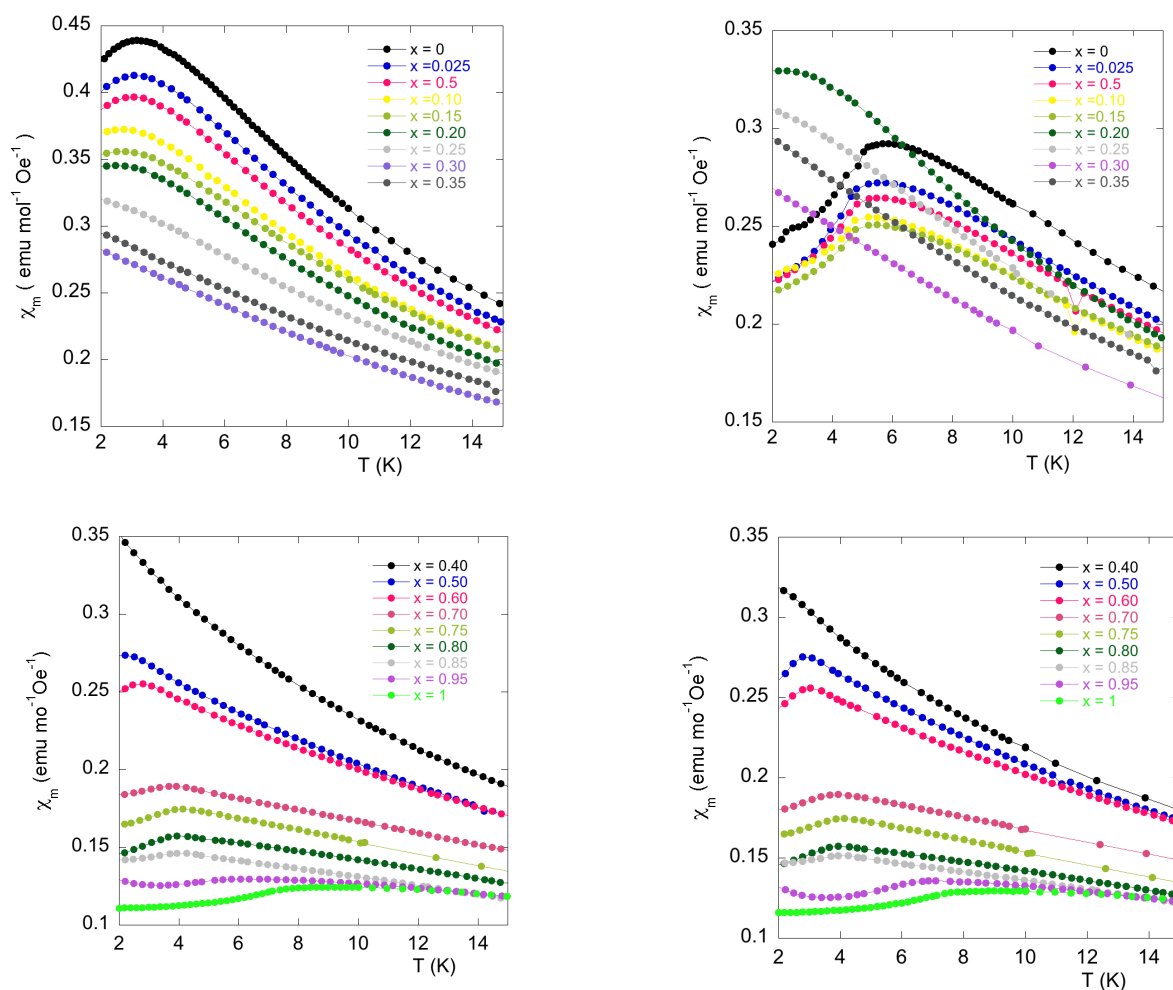


Figure 7: Magnetic susceptibility for the quenched (left) and relaxed (right) phases of (dimim)[FeCl_{1-x}Br_x]₄ ($0 \leq x \leq 1$).

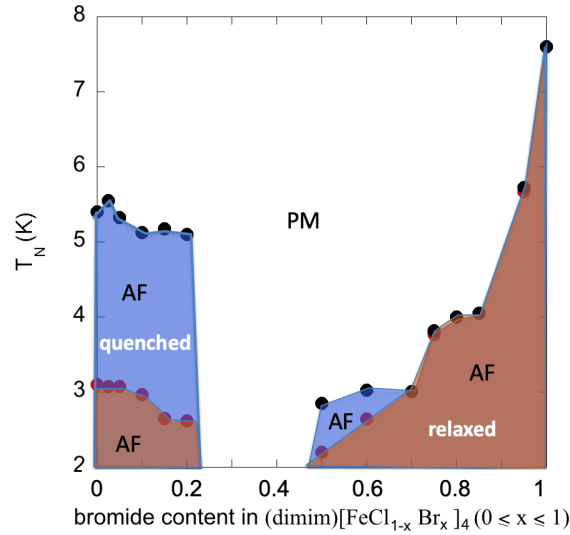


Figure 8: Magnetic phase diagram for both phases of $(\text{dimim})[\text{FeCl}_{1-x}\text{Br}_x]_4$ ($0 \leq x \leq 1$).

Figure 9 left displays the temperature dependence of the molar heat capacity (C_p) of selected samples of the solid solution. The low temperature calorimetric measurements in the absence of an external magnetic field reveal a maximum ($\Delta C_p = 10.6 \text{ J mol}^{-1} \text{ K}^{-1}$) centered at 4.7 K for $(\text{dimim})[\text{FeCl}_4]$. This peak shows the well known λ -shape appearance of a second-order transition and can be associated to a 3D antiferromagnetic order. When the bromide content increases, the peak shifts and broadens (for $x = 0.15$; $\Delta C_p = 0.2 \text{ J mol}^{-1} \text{ K}^{-1}$ centered at 4.5 K), and finally disappears for $x=0.35$ in good agreement with the magnetic measurements. It deserves to be noted that below 30 % of bromide content in the solid solution, the low temperature phases crystallize in the $P2_12_12_1$ space group. Next, a magnetic anomaly in form of a shoulder is detected for $x=0.50$, which becomes a magnetic broad peak when the bromide content is higher than $x = 0.95$ (Figure 9 right). To study this magnetic behavior in detail, we have also measured C_p under a magnetic field of 8 T to plot the difference between the C_p at 0 and 8 T for the $x=0, 0.35, 0.50, 0.60$ and 0.70 compositions (see insets of Figure 9). Although the magnetic difference is small for all samples, this turns into a well-defined peak centered at 3 K for $x = 0.50$. This indicates the presence of some magnetic contributions in such phases, in good agreement with the magnetic susceptibility measurements. The occurrence of this magnetic change could be related with the transformation from long-range magnetic order into short range and could be associated with the occurrence of a structural distortion at low temperature. This solid solution which possesses a crystal structure formed as layers of cations and anions stacked along the b direction is a spatially anisotropic system. The $\text{Fe}\cdots\text{Fe}$ distances inside a layer are shorter than between the layers (the b direction) and thus, the magnetic coupling between the planes are weaker than in the planes.[29] Therefore, the spin correlations must be developed in the planes before the eventual 3D transition. In this way, a simple way to understand the reduction in the amplitude for the specific-heat anomaly, λ -shape appearance of a second-order transition, is to consider the effect of preexisting short-range order at the transition, disappearing the 3D magnetic ordering with the anion substitution, to later it appears again. Hence, the specific-heat anomaly must diminish and appear a broad peak.[40] This effect appears like a shoulder anomaly in the heat capacity and could come from different origins: bidimensional magnetic ordering or short-range magnetic interactions. [41] This means that the effective number of degrees of freedom involved in the 3D order is substantially reduced which could be generated by the increase of chemical pressure in a particular position of the $Ama2$ network. Probably, in the intermediate samples, the substitution of random Cl/Br atoms do not let the occurrence of the phase transition from $Ama2$ to $P2_12_12_1$.

Therefore, the vanishing of the long range magnetic order in this concentration range is due to the change in the exchange coupling interactions.

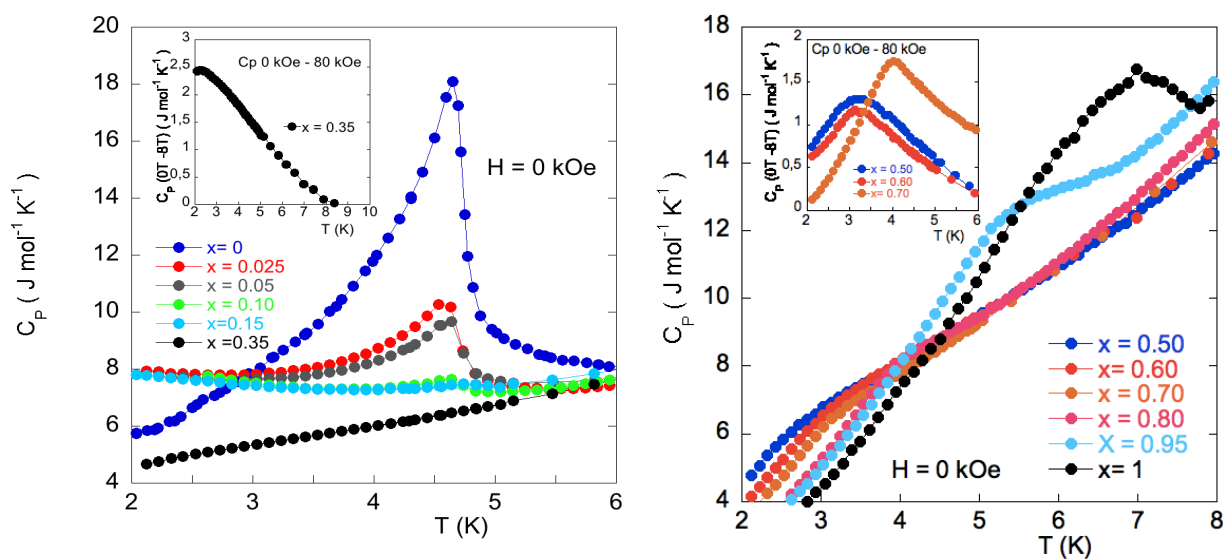


Figure 9: Heat capacity vs. temperature for different Br/Cl ratios at zero magnetic field. The inset shows the difference between the measurements at 0 and 8 T.

5. Conclusion

In summary, a solid solution of eighteen samples, $(\text{dimim})[\text{Fe}(\text{Cl}_{1-x}\text{Br}_x)_4]$ $0 \leq x \leq 1$ was prepared in a one-pot synthesis. The resulting compounds were characterized by single-crystal X-ray and powder synchrotron X-Ray diffraction, being isomorphous with orthorhombic structure (*Ama2* space group) at room temperature. The crystal structure of these imidazolium molten salts can be described as layers of organic cations and inorganic anions extended in the *bc*-plane with an antiparallel stacking along the *a*-axis. The evolution of the cell volume at RT follows the Vegard's law in the whole range of substitution, displaying a non-linear axial expansion in the *b* and *c* direction (shortest Fe \cdots Fe distance). On the other hand, the shortest halide \cdots halide and Fe \cdots centroid distances exhibit a linear expansion with anion substitution. In addition, the melting point and magnetic properties of the solid solution do not follow the expected linear physical behavior. Interestingly, at low temperature different phase transitions have been observed. From $P2_12_12_1$ (**I-a** phase; 0.05-0.25%) to *Ama2* (RT space group remains invariant; 30-60%). Above 60% new structural phase transition is detected. From the magnetic point of view, the 3D magnetic ordering vanishes or falls below 2 K for 25-50% bromide substitution. This phenomenon could be attributed to a modification of the Fe \cdots Fe and Fe \cdots centroid exchange coupling due to the breaking of symmetry after the phase transitions. Although the substitution of bromide by chloride precludes the occurrence of any phase transition for concentrations between 30 and 60%, the origin of this behavior is not clear, moreover considering that the structural parameter at RT follows a linear tendency with the increase of the bromide concentration. To deeply understand the influence of the chemical substitution into the magnetic behavior along this series, neutron powder diffraction on phases with 3D magnetic ordering will be needed.

In conclusion, the physical properties of these isomorphous halometallate molten salts display an unusual physical behavior. The evolution of the melting point and magnetic properties do not obey the expected linear tendency. This phenomenon opens the door to the development and study of new

type of halometallate compounds with novel properties in terms of conductivity, reactivity and magnetism, among others.

Associated Content

*Supporting Information

Experimental data of elemental and thermal analyses, X-ray diffraction, synchrotron X-ray diffraction and magnetic measurements. Crystallographic information (CIF data) can be obtained free of charge from The Cambridge Crystallographic Data Centre via www.ccdc.cam.ac.uk/data_request/cif.

This material is available free of charge via the Internet.

Conflicts of interest

There are no conflicts of interest to declare.

Sample CRediT author statement

Palmerina González-Izquierdo, Oscar Fabelo and Imanol de Pedro: Data curation, Writing-Original draft preparation.

Israel Cano and Oriol Vallcorba: Data curation and Reviewing.

Jesús Rodríguez Fernández and María Teresa Fernández-Díaz: Supervision and Reviewing.

Acknowledgements

Financial support from Universidad de Cantabria (Proyecto Puente convocatoria 2018 financed by SODERCAN_FEDER) and Ministerio de Economía y Competitividad (MAT2017-89239-C2-(1,2)-PID2019-104050RAI00 and MAT2017-83631-C3-3-R). Synchrotron powder diffraction measurements were performed at the ALBA Synchrotron Light Source in Barcelona (proposal nr. 2017092366).

References

- [1] M. Currie, J. Estager, P. Licence, S. Men, P. Nockemann, K. R. Seddon, M. Swadźba-Kwaśny, C. Terrade, C. C., Chlorostannate (II) ionic liquids: speciation, lewis acidity, and oxidative stability. *Inorganic Chemistry*, 52(2012), 1710–1721.
- [2] J. Estager, A. A. Oliferenko, K. R. Seddon, M. Swadźba-Kwaśny. Chlorometallate(III) ionic liquids as lewis acidic catalysts - a quantitative study of acceptor properties. *Dalton Transaction*, 39(2010) 11375–11382.
- [3] S. Hayashi, H. O. Hamaguchi. Discovery of a magnetic ionic liquid [bmim]FeCl₄. *Chemistry Letter*, 33(2004) 1590–1591.
- [4] I. de Pedro, D. P. Rojas, J. Albo, P. Luis, A. Irabien, J. A. Blanco, J. Rodríguez Fernández, Long-range magnetic ordering in magnetic ionic liquid: Emim[FeCl₄]. *Journal of Physics: Condensed Matter*, 22(2010) 296006.

- [5] P. Hao, W. Wang, J. Shen, Y. Fu. Non-transient thermo-/photochromism of iodobismuthate hybrids directed by solvated metal cations. *Dalton Transactions*. 49(2020) 1847-1853.
- [6] M. Armand, F. Endres, D. R. MacFarlane, H. Ohno, B. Scrosati. Ionic-liquid materials for the electrochemical challenges of the future. *Materials For Sustainable Energy: A Collection of Peer-Reviewed Research and Review Articles from Nature Publishing Group*, World Scientific: (2011) 129–137.
- [7] D. Gelman, B. Shvartsev, I. Wallwater, S. Kozokaro, V. Fidelsky, A. Sagy, A. Oz, S. Baltianski, Y. Tsur, Y. Ein-Eli. An aluminum–ionic liquid interface sustaining a durable Al-air battery. *J. Power Sources*. 364(2017) 110–120.
- [8] M. Kar, O. Tutusaus, D. R. MacFarlane, R. Mohtadi. Novel and versatile room temperature ionic liquids for energy storage. *Energy Environment Science*. 12(2019) 566–571.
- [9] M. L. Dietz, C. A. Hawkins. Metal Ion Extraction With Ionic Liquids. *Liquid-Phase Extraction Handbooks in Separation Science*. Elsevier (2020) 539-564.
- [10] X. Feng, X. Xu, Z. Liu, S. Xue, L. Zhang. Novel functionalized magnetic ionic liquid green separation technology coupled with high performance liquid chromatography: A rapid approach for determination of estrogens in milk and cosmetics. *Talanta*, 209(2020) 120542.
- [11] E. Santos, J. Albo, A. Rosatella, C. A. Afonso, A. Irabien. Synthesis and characterization of Magnetic Ionic Liquids (MILs) for CO₂ separation. *Journal of Chemical Technology & Biotechnology* 89(2014) 866–871.
- [12] M. K. Leu, I. Vicente, J. A. Fernandes, I. De Pedro, J. Dupont, V. Sans, P. Licence, A. Gual, I. Cano. On the real catalytically active species for CO₂ fixation into cyclic carbonates under near ambient conditions: Dissociation equilibrium of [BMIm][Fe(NO)₂Cl₂] dependant on reaction temperature. *Applied Catalysis B: Environmental*. 245(2019) 240-250.
- [13] X. Dai, X. Qiang, J. Li, T. Yao, Z. Wang, H. Song. Design and functionalization of magnetic ionic liquids surfactants (MILSs) containing alkyltrimethylammonium fragment. *Journal of Molecular Liquids*. 277(2019) 170-174.
- [14] M. Sajid. Magnetic ionic liquids in analytical sample preparation: A literature review. *TrAC Trends in Analytical Chemistry*. 113(2019) 210-223.
- [15] A. H. M. Fauzi, N. A. S. Amin, R. Mat. Esterification of oleic acid to biodiesel using magnetic ionic liquid: Multi-objective optimization and kinetic study. *Applied Energy*, 114(2014) 809-818.
- [16] F. Scé, I. Cano, C. Martin, G. Beobide, O. Castillo, I. de Pedro. Comparing Conventional and Microwave-Assisted Heating in PET Degradation Mediated by Imidazolium-Based Halometallate Complexes. *New Journal of Chemistry*. 43(2019) 3476- 3485.
- [17] R. L. Vekariya, A review of ionic liquids: applications towards catalytic organic transformations. *Journal of Molecular Liquids*. 227(2017) 44–60.
- [18] I. Cano, C. Martin, J. A. Fernandes, R. W. Lodge, J. Dupont, F. A. Casado-Carmona, W. Lucena, S. Cardenas, V. Sans, I. de Pedro. Paramagnetic ionic liquid-coated SiO₂@Fe₃O₄ nanoparticles—

The next generation of magnetically recoverable nanocatalysts applied in the glycolysis of PET. *Applied Catalysis B: Environmental*, 260(2020) 118110.

[19] J. Kurley, H. Zhang, D. V. Talapin, J. Russell, M. H. Hudson. Halometallate ligand-capped semiconductor nanocrystals. *U.S. Patent No. 10,541,134*. Washington, DC: U.S. Patent and Trademark Office. (2020).

[20] A. M. Buchbinder, H. Abrevaya, G. P. Towler,. Hydrocarbon processes using halometallate ionic liquid micro-emulsions. U.S. Patent Application No. 16/128,151. (2019).

[21] J. Estager, J. D. Holbrey, M. Swadźba-Kwaśny, Halometallate ionic liquids–revisited. *Chemical Society Reviews*, 43(2014) 847-886.

[22] R. D. Rogers, G. Gurau, S. P. Kelley, R. Kore, J. L. Shamshina. Mixed metal double salt ionic liquids with tunable acidity. U.S. Patent No. 10,357,762. (2019).

[23] K. Li, H. Choudhary, M. K. Mishra, R. D. Rogers. Enhanced Acidity and Activity of Aluminum/Gallium-Based Ionic Liquids Resulting from Dynamic Anionic Speciation. *ACS Catalysis*. 9(2019), 9789-9793.

[24] H. Niedermeyer, J. P. Hallett, I. J. Villar-Garcia, P. A. Hunt, T. Welton. Mixtures of ionic liquids. *Chemical Society Reviews*. 41(2012) 7780– 7802.

[25] G. Chatel, J. F. B. Pereira, V. Debbeti, H. Wang, R. D. Rogers. Mixing ionic liquids – “simple mixtures” or “double salts”? *Green Chemistry*. 16(2014) 2051–2083.

[26] Y. L. Wang, B. Li, S. Sarman, F. Mocci, Z. Y. Lu, Y. Yuan, A. Laaksonen, M. D. Fayer. Microstructural and Dynamical Heterogeneities in Ionic Liquids. *Chemical Reviews*. (2020) doi.org/10.1021/acs.chemrev.9b00693.

[27] N. S. M. Vieira, I. Vázquez-Fernández, J. M. M. Araújo, N. V. Plechkova, K. R. Seddon, L. P. N. Rebelo, A. B. Pereiro, A. B. Physicochemical Characterization of Ionic Liquid Binary Mixtures Containing 1-Butyl-3-methylimidazolium as the Common Cation. *Journal of Chemical & Engineering Data*. 64(2019), 4891-4903.

[28] Y. Yoshida, J. Fujii, K. Muroi, A. Otsuka, G. Saito, M. Takahashi, T. Yoko. *Synthetic metals*. 153(2005) 421-424.

[29] A. García-Saiz, I. de Pedro, P. Migowski, O. Vallcorba, J. Junquera, J. A. Blanco, O. Fabelo, D. Sheptyakov, J. C. Waerenborgh, M. T. Fernández-Díaz, J. Rius, J. Dupont, J. A. González, J. Rodríguez Fernández. Anion– π and Halide–Halide Nonbonding Interactions in a New Ionic Liquid Based on Imidazolium Cation with Three-Dimensional Magnetic Ordering in the Solid State. *Inorganic chemistry*, 53(2014), 8384-8396.

[30] A. García-Saiz, P. Migowski, O. Vallcorba, J. Junquera, J. A. Blanco, J. A. González, M. T. Fernández-Díaz, J. Rius, J. Dupont, J. Rodríguez Fernández, I. de Pedro. A Magnetic Ionic Liquid Based on Tetrachloroferrate Exhibits Three-Dimensional Magnetic Ordering: A Combined Experimental and Theoretical Study of the Magnetic Interaction Mechanism. *Chemistry–A European Journal*, 20(2014) 72-76.

- [31] Bruker. SAINT. Bruker AXS Inc., Madison, Wisconsin, USA (2012).
- [32] Bruker. *SADABS*. Bruker AXS Inc., Madison, Wisconsin, USA (2001).
- [33] G. M. Sheldrick, Crystal structure refinement with SHELXL. *Acta Crystallographica Section C: Structural Chemistry*, 71(2015) 3-8.
- [34] F. Fauth, I. Peral, C. Popescu, M. Knapp. The new material science powder diffraction beamline at ALBA synchrotron. *Powder Diffraction*, 28(2013) S360-S370.
- [35] J. Rodríguez-Carvajal, Juan. "FullProf." *CEA/Saclay, France* (2001).
- [36] I. de Pedro, O. Fabelo, A. García-Saiz, O. Vallcorba, J. Junquera, J. A. Blanco, J. C. Waerenborgh, D. Andreica, A. Wildes, M. T. Fernández-Díaz, J. Rodríguez Fernández. Dynamically slow solid-to-solid phase transition induced by thermal treatment of DimimFeCl₄ magnetic ionic liquid. *Physical Chemistry Chemical Physics*, 18(2016) 21881-21892.
- [37] A. R. Denton, N. W. Ashcroft. Vegard's law. *Physical review A*, 43(1991) 3161-3164.
- [38] A. García-Saiz, I. de Pedro, O. Vallcorba, P. Migowski, I. Hernández, L. F. Barquin, I. Abrahams, M. Motevalli, J. Dupont, J. A. Gonzalez, J. Rodríguez Fernández. 1-Ethyl-2, 3-dimethylimidazolium paramagnetic ionic liquids with 3D magnetic ordering in its solid state: synthesis, structure and magneto-structural correlations. *RSC Advances*, 5(2015), 60835-60848.
- [39] P. González-Izquierdo, O. Fabelo, G. Beobide, I. Cano, I. R de Larramendi, O. Vallcorba, J. Rodríguez Fernández, M. T. Fernández-Díaz, I. de Pedro. Crystal structure, magneto-structural correlation, thermal and electrical studies of an imidazolium halometallate molten salt:(trimim)[FeCl₄]. *RSC Advances*, 10(2020), 11200-11209.
- [40] I. de Pedro, J. M. Rojo, J. Rodríguez Fernández, M. T. Fernández-Díaz, T. Rojo. Sinusoidal magnetic structure in a three-dimensional antiferromagnetic Co₂(OH)AsO₄: Incommensurate-commensurate magnetic phase transition. *Physical Review B*, 81(2010), 134431.
- [41] P. Sengupta, A. W. Sandvik, R. R. P. Singh. Specific heat of quasi-two-dimensional antiferromagnetic Heisenberg models with varying interplanar couplings. *Physical Review B*, 68(2003), 094423.